Space Weather

RESEARCH ARTICLE
10.1029/2022SW003104

Ionospheric Response to the M- and X-Class Solar Flares of 28 October 2021 Over the African Sector

John Bosco Habarulema[1,2], Mpho Tshisaphungo[1], Zama Thobeka Katamzi-Joseph[1,2], Tshimangadzo Merline Matamba[1], and Rendani Nndanganeni[1]

[1]South African National Space Agency (SANSA), Hermanus, South Africa, [2]Department of Physics and Electronics, Rhodes University, Makhanda, South Africa

Key Points:

- The M2.2 class solar flare caused total electron content increase reaching 12% over background variability in mid latitudes
- The effect on high frequency (HF) communication through the E and F1 layers lasted about 2 hr (1025–1215 UT) following the M2.2 class solar flare
- Overall, HF propagation modes requiring both F and E layers were restricted during the duration of all the three studied solar flares

Supporting Information:

Supporting Information may be found in the online version of this article.

Correspondence to:

J. B. Habarulema,
jhabarulema@sansa.org.za

Citation:

Habarulema, J. B., Tshisaphungo, M., Katamzi-Joseph, Z. T., Matamba, T. M., & Nndanganeni, R. (2022). Ionospheric response to the M- and X-class solar flares of 28 October 2021 over the African sector. *Space Weather*, *20*, e2022SW003104. https://doi.org/10.1029/2022SW003104

Received 24 MAR 2022
Accepted 5 AUG 2022

Abstract On the 28 October 2021, a total of thirteen solar flares occurred. Of these, there were two M- and one X-class solar flares while the rest fell within the C-class category. The first and second M-class flares peaked at 0740 UT and 1028 UT, respectively, while the X1.0 class reached the peak at 1535 UT. While it is known that strong solar flares cause total absorption of frequencies in the high frequency (HF) range, the F2 layer was consistently present on 28 October 2021 as shown by the critical frequency of the F2 layer (foF2). However, using South African ionosonde data over Hermanus (34.4°S, 19.2°E) and Grahamstown (33.3°S, 26.5°E), we show that the lower frequencies in the E and F1 layers were the most affected by the M-class solar flares. Following the peak of the M2.2 solar flare at 1028 UT, an enhancement reaching about 12% over the background in total electron content (TEC) is observed on 28 October 2021 especially in the Southern hemispheric part of the African sector within the latitude range of 20°–40°S. In response, mid latitude ionosonde data showed that there were no echoes from the E and F1 layers for about 2 hr during ≈1025–1225 UT, restricting complex modes of HF communication such as double hops (1F1E) utilizing a combination of more than one ionospheric layer.

Plain Language Summary Solar flares are one of the natural space weather phenomena which influence atmospheric composition on short time scales and can lead to strong effects causing degradation or absence of some space based applications. Within the ionized part of the Earth's atmosphere usually known as the ionosphere, M and X class flares cause minor to major radio blackout implying that skywave communication using high frequencies is directly affected. This is due to the ionization of the D region which is the lower layer of the ionosphere. Therefore, studies of solar flares' effects on Earth's atmosphere are useful for both fundamental and practical applications involving radio communication, as well as positioning and navigation purposes.

1. Introduction

Ionospheric effects due to solar flare occurrence have been widely studied over decades (for earlier literature and a detailed review, see Mitra, 1974; Prölss, 2004) and range from partial or total radio blackout for high frequency (HF) communication (e.g., Barta et al., 2019; Curto et al., 2018; Davies, 1990; McNamara, 1991; Mosna et al., 2020; Prölss, 2004, and references therein) to long-term orbital decay for Low Earth Orbit satellites as a result of atmospheric expansion arising from increased ionization. It has also been shown/stated that a combination of atmospheric expansion and intense solar flare radio emissions lead to degradation of satellite communications, such as for Global Navigation Satellite Systems (GNSS) constellations and thus influence their precision abilities (e.g., Davies, 1990; Yasyukevich et al., 2018). Solar flares are usually classified according to the peak intensity of X-ray flux in the energy range of 0.1–0.8 nm as A, B, C, M and X class. It is now relatively understood that the first three classes (A, B and C) have little influence on the Earth's atmospheric effects especially on high frequency communication while the M- and X-class solar flares lead to varying magnitudes in ionospheric behavior on the sunlit side of the Earth (e.g., Barta et al., 2019; Blagoveshchensky & Sergeeva, 2019; Curto et al., 2018; Davies, 1990; Fagundes et al., 2020; Mosna et al., 2020; Yasyukevich et al., 2018, and references therein). According to the United States' National Oceanic and Atmospheric Administration (NOAA), the largest recorded solar flare in history was on 4 November 2003 (X28) and it led to the saturation of the Geostationary Operational Environmental Satellite (GOES) detectors. The magnitude of this solar flare has since been suggested to have reached X45 (Thomson et al., 2004) meaning that the X-ray flux reached 4.5 mW/m^2 instead of the earlier reported value of 2.8 mW/m^2. Using ionosonde data over Europe and South Africa, Barta et al. (2019)

presented ionospheric effects as a result of the X- and M-class solar flares during the solar cycle 23. Their results showed that partial or total radio blackout was observed over all locations for flares of intensity greater than M6, with complete fadeout ranging between 0.25 and 2.5 hr. From early 2000s, ionospheric response studies to solar flares' occurrence have benefited from the increasing number of GNSS observations (García-Rigo et al., 2007; Habarulema et al., 2020; Le et al., 2013; Tsurutani et al., 2005, 2009; Yasyukevich et al., 2018). For-example, in their theory and observations study, Liu et al. (2004) showed that the rate of change of TEC can serve as a demonstrator of the sudden variations in flare radiations. A solar flare detection system was developed based on TEC derived from GPS observations (García-Rigo et al., 2007). Le et al. (2013) presented the ionospheric response during about 100 X-class solar flares from 1999 to 2006 based on GNSS derived TEC among other data sources. A relatively detailed review of solar flare effects and other energetic particles on the ionosphere is presented in Tsurutani et al. (2009). Tsurutani et al. (2005) compared the solar flare events of 28 October 29 (X17), 29 October (X7), 4 November (X28) in 2003 and 14 July 2000 (X10). These authors reported that TEC increase after the onset of the 28 October 2003 solar flare lasted up to three hours way beyond the duration of the solar flare of about 1.5 hr (0951–1124 UT). Contrary to the belief that the solar flares affect the Earth's atmosphere where the radiation is absorbed, it has recently been shown that its influence extends to the geospace through electrodynamic coupling of the ionosphere-magnetosphere during the X9.3 solar flare of 6 September 2017 (Liu, Qian, et al., 2021; Liu, Wang, et al., 2021). Thus understanding solar flare effects on ionosphere and generally Earth's atmosphere remains relevant and useful for both fundamental and practical applications. In this paper, we present the ionospheric variability over the African sector when multiple solar flares occurred on 28 October 2021 based on TEC derived from GNSS observations as well as ionospheric parameters extracted from South African ionosonde data over Grahamstown (33.3°S, 26.5°E) and Hermanus (34.4°S, 19.2°E). GNSS derived TEC changes are considered within latitude and longitude ranges of 40°S–50°N and 20°–40°E, respectively.

2. Data Sources and Methodology

2.1. GNSS Data

GNSS receiver locations within latitude and longitude ranges of 40°S–50°N and 20°–40°E, respectively, have been considered for analysis. TEC from GPS observations is derived with algorithm which assumes the ionosphere as a spherical shell of height 350 km (Seemala & Valladares, 2011), and an elevation threshold of 15° is applied to minimize multipaths errors. A 15° threshold is chosen to retain significant data coverage in terms of latitude and longitude especially over the African sector with sparsely distributed GNSS receivers (Habarulema et al., 2020). The impact of the solar flares on TEC is studied using two approaches based on regional and individual location analyses:

1. First, to identify the regional effects of the solar flares on ionospheric TEC, we first fit TEC data for each visible satellite (PRN) over all locations within the defined spatial resolutions to a fourth order polynomial. This is followed by subtracting fitted TEC from actual TEC data providing TEC perturbations (hereafter known as ΔTEC). This method removes diurnal TEC variability (e.g., Valladares et al., 2009) and has been shown to clearly reveal TEC changes on a regional scale in response to solar flare occurrence (Habarulema et al., 2020). Two-dimensional ΔTEC plots as a function of latitude and time are then generated on 28 October 2021 and 27 October 2021 (second geomagnetically quiet day in the month) for a longitude sector of 20° (20°–40°E) within latitude range of 40°S–50°N.
2. Second, the solar flare effects on TEC at different latitude locations are identified by benchmarking TEC variability on 28 October 2021 with the median of the most four quiet days of the month. The geomagnetically quiet days of the month (in their order of "quietness") were 28, 27, 29, 7 and 23 October 2021. Out of these, the 28 October 2021 (subject of this study) was removed and thus computation of the median TEC values (which served as the background) was done for four days. The deviation between TEC on 28 October 2021 and median values were computed using

$$\text{Deviation} = \left(\frac{\text{TEC} - \text{TEC}_{\text{median}}}{\text{TEC}_{\text{median}}}\right) \times 100\%$$

Table 1
Geographic Coordinates of the GNSS Receiver Locations Used for Diurnal TEC Analysis on 28 October 2021

Station, country	Station code	Latitude	Longitude	Magnetic latitude
Grahamstown, South Africa	GRMA	−33.3	26.5	−42.34
Hermanus, South Africa	HNUS	−34.4	19.2	−41.95
Zambia, Zambia	ZAMB	−15.4	28.3	−26.24
Malindi, Kenya	MAL2	−3.0	40.2	−12.42
Ramo, Israel	RAMO	30.6	34.8	23.37
Mersin, Turkey	MERS	36.6	34.3	30.48

where TEC and TEC_{median} represent TEC on 28 October 2021 and median of the four geomagnetically quiet days of 7, 23, 27 and 29 October 2021, respectively. Table 1 presents details about GNSS locations used for the diurnal TEC analysis.

Figure 1 shows the location of GNSS receivers (black dots) and ionosondes (red dots) used in this study. The vertical dashed red lines indicate the longitude sector 20–40°E used for regional TEC investigations during the times of solar flare occurrence.

2.2. Ionosonde Data

To investigate the solar flares' effects on different layers of the ionosphere, we have utilized South African ionosonde data over Hermanus (34.4°S, 19.2°E) and Grahamstown (33.3°S, 26.5°E). As far as we know, these were the only operational African ionosondes on 28 October 2021. In addition to visualization of ionograms, we have extracted values of critical frequencies for E, F1 and F2 layers for further analysis. Because the solar flares peak times were 0740, 1028 and 1535 UT for M1.4, M2.2 and X1.0, respectively, most of the African sector was within the sunlit exposure and thus appropriate for investigating its effects on E, F1 and F2 layers. The ionosonde data were also used to derive bottomside total electron content (BTEC) which provided an independent validation of the observations made from GNSS derived data during the solar flares' duration. Bottomside TEC (BTEC) is derived by integrating ionosonde measured electron density up to the maximum height of the F2 layer (hmF2) peak at 5 min cadence as follows;

$$\mathrm{BTEC} = \int_{\sim 90}^{\mathrm{hmF2}} N_e ds$$

where N_e is the electron density. In the above integration, the lower limit is the approximate start of the E layer or depending on data availability as the ionosonde does not measure the *D* layer. Therefore the derived BTEC used in this study does not include the modeled topside contribution to TEC as explained in Huang and Reinisch (2001).

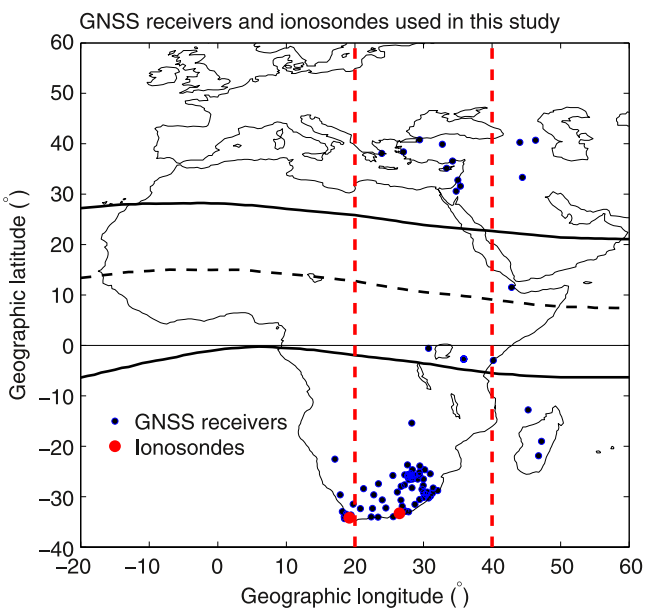

Figure 1. Distribution of GNSS receivers (blue dots) and ionosondes (red dots) used in this study. The vertical dashed red lines indicate the 20° longitude sector (20–40°E) considered for total electron content analyses.

2.3. Solar Wind and X-Ray Flux Data

The solar wind conditions during the solar flares occurrence were examined by considering 1 min data for solar wind velocity, Bz component of the interplanetary magnetic field (IMF Bz) and solar wind dynamic pressure. Data for these parameters were accessed from the OMNI database (https://spdf.gsfc.nasa.gov/pub/data/omni/high-res-omni/) which provides shifted solar wind information after accounting for time propagation delay from the L1 point to the magnetosphere's bow shock nose.

The strengths of the solar flares on 28 October 2021 are identified from the peak intensities of X-ray flux in the energy range of 0.1–0.8 nm provided by the Geostationary Operational Environmental Satellite (GOES 16). GOES X-ray data at 1 min resolution can be found on http://www.ngdc.noaa.gov/stp/satellite/goes/index.html.

3. Results

On the 28 October 2021, a total of thirteen solar flares occurred. Of these, there were ten, two and one C, M and X class solar flares, respectively. Table 2 shows the start and end times of these flares including their source region on the Sun. The M and X class solar flares used in the analysis presented in this paper are indicated in bold. Figure 2a shows the GOES 16 X-ray flux at 1 min resolution on 27–28 October 2021. The left and right *y*-axes show the X-ray flux and solar flare class, respectively. The GOES X-ray flux data shows that

Table 2
Solar Flares Which Occurred on 28 October 2021

Solar flare	Region of origin	Start time (UT)	End time (UT)	Peak time (UT)	Duration (min)
C1.2	2887	0132	0145	0138	13
M1.4	**2887**	**0730**	**0745**	**0740**	**15**
C1.1	2887	0956	1005	1000	9
M2.2	**2887**	**1019**	**1037**	**1028**	**18**
C1.2	2887	1209	1227	1217	18
C2.3	2891	1226	1250	1238	34
C3.3	2887	1314	1325	1321	11
C3.9	2887	1346	1405	1359	19
X1.0	**2887**	**1517**	**1548**	**1535**	**31**
C3.2	2891	1807	1815	1810	8
C3.2	2891	1934	1947	1945	13
C3.2	2891	1947	1957	1953	10
C1.6	2891	2102	2111	2107	9

Note. Source: https://www.spaceweatherlive.com/en/archive/2021/10/28/xray.html. Ionospheric variability is investigated during the M and X flares indicated in bold.

the M1.4, M2.2 and X1.0 solar flares peaked at 0740, 1028 and 1535 UT, respectively and are indicated in Figure 2a.

Figure 2b shows variations of the solar wind velocity, Vsw (blue curve) and Bz component of the interplanetary magnetic field, IMF Bz (black curve) while the Dst index (blue curve) and solar wind dynamic pressure (black curve) are shown in Figure 2c for 27–28 October 2021. The red vertical lines in Figures 2b-2c show the peak times for the M1.4, M2.2 and X1.0 solar flares, respectively. The Interplanetary and geophysical conditions were largely quiet during the 27–28 October 2021. In particular, Vsw was below the typical average value of 350 km/s for the 28 October 2021 when the solar flares under study occurred, while Bz fell within ±3 nT. The Dst index also show quiet conditions ($-3 \leq$ Dst ≤ 16 nT) and the maximum Kp index (not shown) was below 2 for both 27 and 28 october 2021. During the duration of the three solar flares, the solar wind dynamic pressure (P_{sw}) was mostly below 2 nPa and had the highest value of 2.11 nPa at the end of the X1.0 solar flare.

To identify solar flare effects on TEC observations, we first fit TEC data for each satellite (PRN) to a fourth order polynomial. This is followed by subtracting fitted TEC from actual TEC data providing TEC perturbations (hereafter known as ΔTEC). This procedure is demonstrated in Figure 3a over Malindi, MAL2 (3.0°S, 40.2°E) and Hermanus, HNUS (34.4°S, 19.2°E) using TEC data for satellites (PRNs) 3 and 7 during the time when the M2.2 class solar flare occurred. In Figure 3a, the actual and fitted TEC data are plotted as blue and red curves, respectively. Figure 3b shows ΔTEC over MAL2 and HNUS, respectively. The vertical red lines on ΔTEC panels show the peak time of the M2.2 class solar flare at 1028 UT. The procedure in Figures 3a-3b is repeated for all visible satellites over all GNSS receiver locations under consideration and the resulting ΔTEC data is then binned within latitudinal and temporal resolutions of 3° × 6 min and median ΔTEC selected in each bin for all ΔTEC data within the longitude range of 20–40°E. Figure 3c shows the two dimensional ΔTEC plot as a function of latitude and time within the longitude sector covering 20° for 28 October 2021. To compare with data during the day without significant solar flare occurrence to alter electron density variability, Figure 3d is similar to Figure 3c for 27 October 2021. Only C-class solar flares occurred on 27 October 2021 with maximum being C8.51 during 0547–0620 UT, a time period when electron density is low to observe any influence of the flare activity. The vertical black lines in Figure 3c show the peak times of the solar flares on 28 October 2021 at 0740, 1028 and 1535 UT for the M1.4, M2.2 and X1.0 solar flares, respectively. Vertical lines are also inserted in Figure 3d for 27 October 2021 for direct comparison with observations in Figure 3c. Comparing observations on 27 and 28 October 2021, simultaneous TEC increase can be seen during the peaktime of the M2.2 solar flare. This observation is largely clear between around 0°–40°S where sufficient data is available, and is in fact clearly demonstrated by ΔTEC results in Figure 3b over MAL2 and HNUS. For example, maximum ΔTEC values over MAL2 and HNUS are 0.625 TECU and 0.541 TECU at 1031 UT (3 min after the peaking of the M2.2 solar flare) in Figure 3b. In the northern hemispheric part, available data shows enhanced TEC just after 20°N to about 35°N around the peak time of the M2.2 solar flare. Comparatively, such TEC enhancement at about 1030 UT time is not evident in Figure 3d on 27 October 2021. For the X1.0 class solar flare which peaked at 1535 UT, the TEC increase is more clearer for the southern (about 15°–35°S) than northern hemispheric part of the African sector (despite limited data). There is TEC increase (see Figure 3d around 5°–40°S) just after 1600 UT on 27 October 2021. While this increase has not been investigated in details, we note in passing that there was a C2.1 class solar flare during 1621–1644 UT (lasting 23 min). We however note that available data does not show clear corresponding TEC increase in the northern hemisphere on 27 October 2021 after 1600 UT.

Furthermore, Figure 3c shows TEC depletion around the peak of X1.0 solar flare at ≈5–15°S and ≈25–40°N in the southern and northern hemispheres, respectively. This geographic latitude range is roughly equivalent to ≈15–25°S and ≈15–30°N geomagnetic latitude. Thus, available data shows that the start of the TEC depletion is around the crest of the equatorial ionization anomaly region. No clear TEC depletion is observed at these latitude

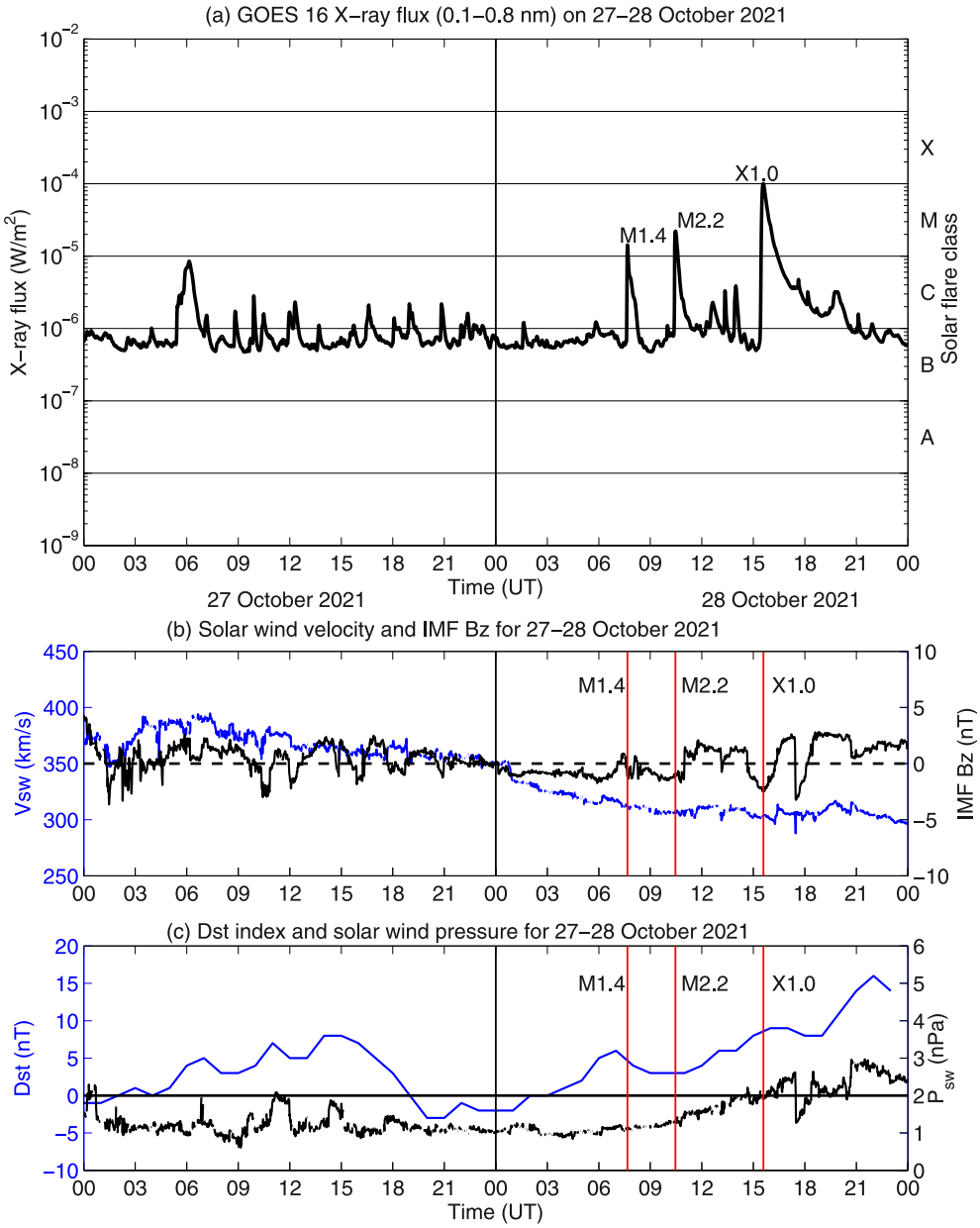

Figure 2. Changes in (a) one minute X-ray flux (W/m^2) data from the Geostationary Operational Environmental Satellite (GOES 16), (b) solar wind velocity (blue curve) and Bz component (black curve) of the interplanetary magnetic field (IMF Bz); and (c) Dst index (blue curve) and solar wind dynamic pressure (black curve) for 27–28 October 2021. The vertical red lines in (b) and (c) show the peak times for the M1.4, M2.2 and X1.0 solar flares, respectively on 28 October 2021.

ranges during the duration of the M1.4 and M2.2 solar flares. The M1.4 solar flare started when the IMF Bz was in the northward direction with gradual change toward the southward direction. The IMF Bz turned southward at 0735 UT (4 min after the commencement of the flare) and remained southward until 0803 UT, having reached a maximum value of −1.37 nT at 0742 UT. Both M2.2 and X1.0 solar flares occurred when IMF Bz was consistently southward. For M2.2 flare (1019–1037 UT), the IMF Bz was already southward before the flare and was infact in this polarity even before 1000 UT and turned northward at 1100 UT. A similar scenario is true for the X1.0 flare (1517–1548 UT) where IMF Bz was southward between 1440 and 1615 UT and only turned northward at 1616 UT for the rest of the day. It is known that the decrease of southward IMF Bz and its northward turning creates conditions favorable for reduced Region 1 field aligned currents that may result into westward disturbance electric field in low latitude regions during daytime (e.g., Kelley et al., 1979; Zhang et al., 2017). We however

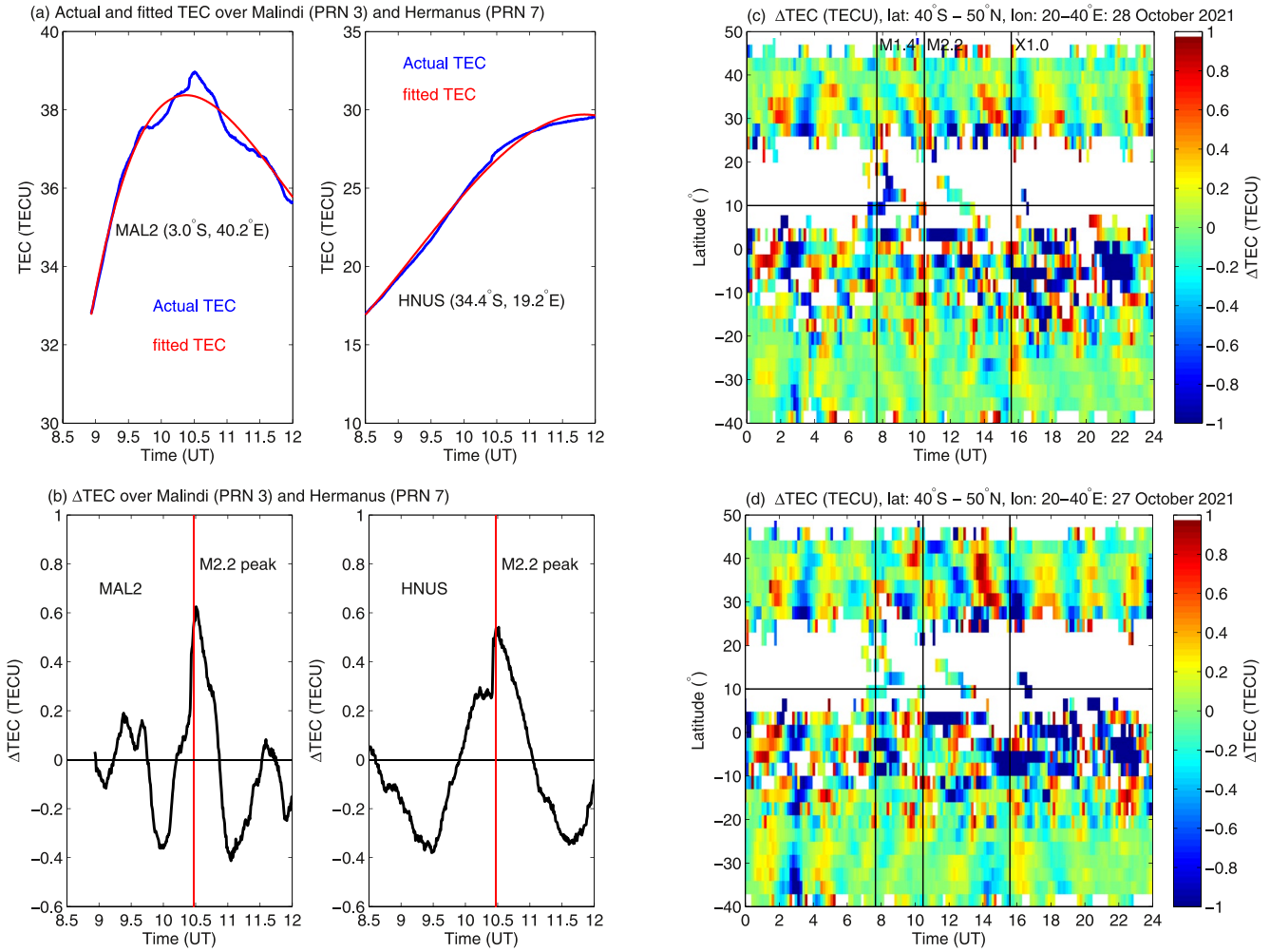

Figure 3. Panels in (a) show the procedure of determing total electron content (TEC) perturbations (ΔTEC) by fitting actual TEC data (blue curve) to a fourth order polynomial yielding fitted TEC (red curve) over low and mid latitude locations Malindi, MAL2 (3.0°S, 40.2°E) and Hermanus, HNUS (34.4°S, 19.2°E). Panels in (b) are the respective ΔTEC (actual TEC - fitted TEC) values over MAL2 and HNUS. Two dimensional ΔTEC changes covering latitude and longitude ranges of 40°S–50°N and 20–40°E for (c) 28 October 2021 and (d) 27 October 2021. The horizontal black line in (c)–(d) approximate the location of the geomagnetic equator while the three vertical black lines show the peak times of 0740, 1028 and 1535 UT for the M1.4, M2.2 and X1.0 solar flares, respectively.

note that this day was geomagnetically quiet (Kp < 2) and the IMF Bz fluctuations in Figure 2b were small in magnitudes (±3 nT). The solar wind dynamic pressure was also considerably small during the duration of the solar flares with maximum of 2.11 nPa at the end (1548 UT) of X1.0 solar flare. With these conditions, we think that the solar wind-magnetosphere coupling may not have influenced the observed TEC depletion around the peak of the X1.0 solar flare on 28 October 2021 (Figure 3c). In a previous study, Zhang et al. (2017) concluded that consistent southward polarity of IMF Bz with magnitude smaller than −4 nT and solar wind pressure of 2 nPa should not have influence on ionospheric equatorial electrodynamics with origin from the solar wind and magnetosphere. The observed TEC depletion at the peak of X1.0 solar flare in low latitudes may therefore be related to the ionospheric electrodynamics associated with the solar flare occurrence (e.g., Chen et al., 2021; Liu, Qian, et al., 2021; Liu, Wang, et al., 2021; Zhang et al., 2017). A similar TEC depletion which started just after 0300 UT and prevailed until 1700 UT (especially in the southern hemisphere) observed in Figure 3d on 27 October 2021 covered ≈15–20°S and ≈15–25°N geomagnetic latitude. The cause of this is not clear, although there was a C2.1 solar flare which started at 1621 UT and lasted for 23 min. This aspect requires further investigation.

Figure 4 shows a comparison of diurnal TEC on 28 October 2021 and median TEC values on the four geomagnetically quiet days in October 2021 within the longitude sector 20–45°E for mid latitude locations in southern and northern hemispheres as well as mid-low latitude and low latitudes. The vertical black lines indicate the peak

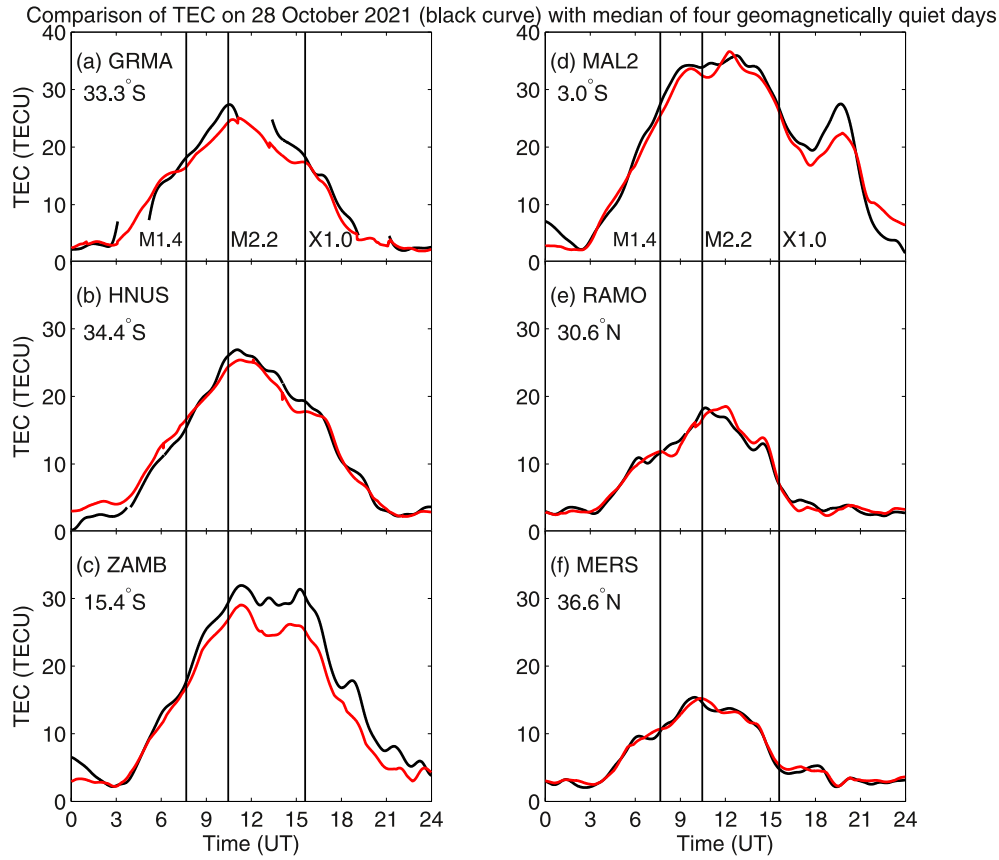

Figure 4. Diurnal variation of total electron content (TEC) over different GNSS locations on 28 October 2021 (black curve) compared to median TEC values (red curve) on four geomagnetically quiet days of 27, 29, 7 and 23 October 2021.

times 0740, 1028 and 1535 UT for M1.4, M2.2 and X1.0 solar flares, respectively. At the peak time of the M2.2 solar flare, clear TEC increase over the median values can be seen over mid- and mid-low latitude region in the southern hemisphere with percentage deviation values of 12%, 7% and 10% at Grahamstown (33.3°S, 26.5°E), Hermanus (34.4°S, 19.2°E) and Zambia (34.4°S, 19.2°E), respectively. This was TEC increase of 3 TECU, 1.6 TECU and 2.5 TECU for Grahamstown, Hermanus and Zambia, respectively at the peak time of the M2.2 solar flare. At this time, the deviation at the low latitude location, Malindi (3.0°S, 40.2°E) was 4%. In the northern hemisphere, the deviations were 8% and −4% over RAMO (30.6°N, 34.8°E) and MERS (36.6°N, 34.3°E), respectively at the peak time of the M2.2 solar flare. Higher deviation of 20% at the peak time of X1.0 flare was observed over the mid-low latitude Zambia location. Corresponding deviation values over Grahamstown and Hermanus were 5% and 9%, respectively.

Figure 5 shows the diurnal bottomside TEC over (a) GR13L and (b) HE13N on 28 October 2021 compared to the median of the four geomagnetically quiet days in October 2021. The vertical black lines show peak times for the M1.4, M2.2 and X1.0 solar flares respectively. BTEC was elevated above the median background for most of the time after the peak time of the M2.2 solar flare until the peak time of the X1.0 flare. Quantitatively, the average BTEC increases just after the peak time of the M2.2 solar flare until 1200 UT (a period characterized by absence of HF echoes from the E and F1 layers, see Figure 8) are 13% and 8% over GR13L and HE13N, respectively. Based on the four most quiet days of October 2021, these average BTEC increases are almost twice the maximum day-to-day variability average which reach about 6 TECU and 4 TEC over GR13L and HE13N, respectively during the same time period. Within 10 min after the M2.2 solar flare peak, BTEC deviation reached 24% and 20% over GR13L and HE13N at 1030 UT and 1035 UT, respectively. Interestingly, these average BTEC increase values are consistent with what was obtained from GPS TEC observations over the same locations at the M2.2 solar flare peak time. The differences in TEC increase over GR13L (26.5°E) and HE13N (19.2°E) may be

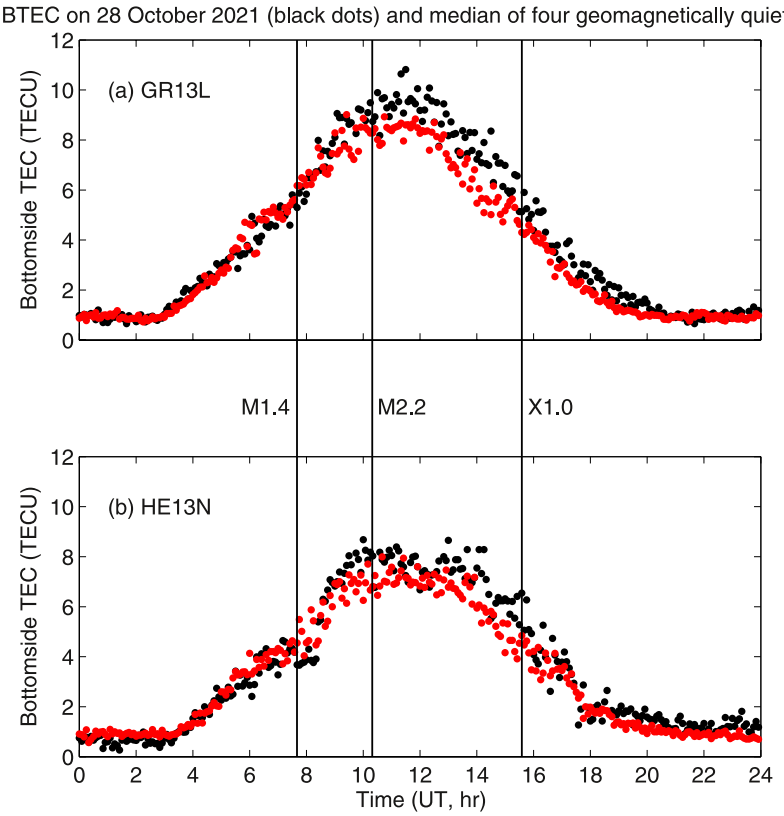

Figure 5. Diurnal variation of total electron content (BTEC) on 28 October 2021 (black dots) over (a) Hermanus (34.4°S, 19.2°E) and (b) Grahamstown (33.3°S, 26.5°E). The red dots show median BTEC for the four geomagnetically quiet days of 7, 23, 27 and 29 October 2021. The vertical black lines indicates the peak times of the M1.4, M2.2 and X1.0 solar flares at 0740, 1028 and 1535 UT, respectively.

due to actual local time over each location as their time difference is about 30 min. At the peak of the M2.2 solar flare, the local times at GR13L and HE13N were 1214 LT and 1145 LT, respectively.

For practical application purposes, the question to address is whether such TEC increases in the range 5%–12% (for the M2.2 solar flare) in mid latitudes results into any influence on HF communication. To partly address this, we analyze ionosonde data over GR13L and HE13N focusing on ionograms and critical frequencies of E, F1 and F2 layers.

Figure 6 shows ionograms over HE13N and GR13L during the time period of the M1.4 solar flare which occurred between 0730 and 0745 UT. The ionograms are shown at 15 min intervals from 0730 to 0800 UT. Over HE13N (a-c), HF echoes from the F1 and F2 layers were present during the whole duration of this solar flare. Ionogram data at 5 min intervals (not shown here but in supporting information) show that there were no echoes from the E-region during 0740–0750 UT. For GR13L, HF echoes from both E and F1 layers disappeared for 10 min and recovered at 0800 UT. GR13L ionogram data show that data from E and F1 layers were available at 0735 UT and 0755 UT (not shown, see Supporting Information S1).

Figure 7 shows examples of ionograms over HE13N (a–c) and GR13L (d–f) demonstrating the effect of the M2.2 solar flare on E and F1 layer frequencies at 1030, 1100 and 1115 UT on 28 October 2021. Given that there were HF echoes from both E and F1 layers at 0800 UT (see Figures 6c and 6f), it is evident that their absence at 1030, 1100 and 1115 UT that correspond to approximately 1230, 1300 and 1315 local time, respectively is due to the ionization due to the solar flare within the *D* region. The solar flare causes D-region ionization in the sunlit hemisphere resulting into unusually higher electron densities contributing to the absorption of the low frequencies within the HF band. Most remarkably is the significant diminishing of the ordinary (O) and extra-ordinary (X) traces at 1030 UT over HE13N as shown in Figure 7a.

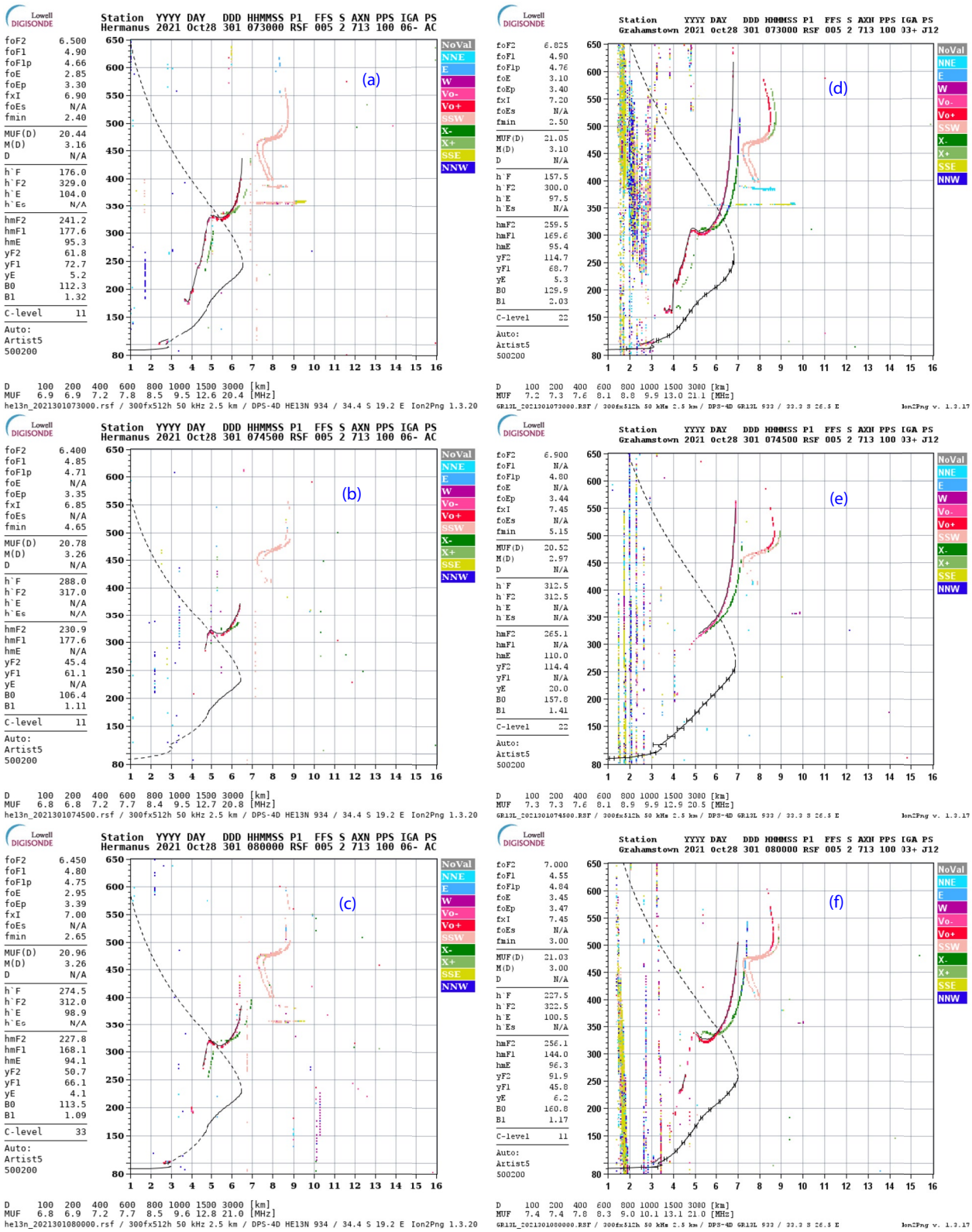

Figure 6. Ionograms over HE13N (a–b) and GR13L (d–f) on 28 October 2021 from 0730 to 0800 UT.

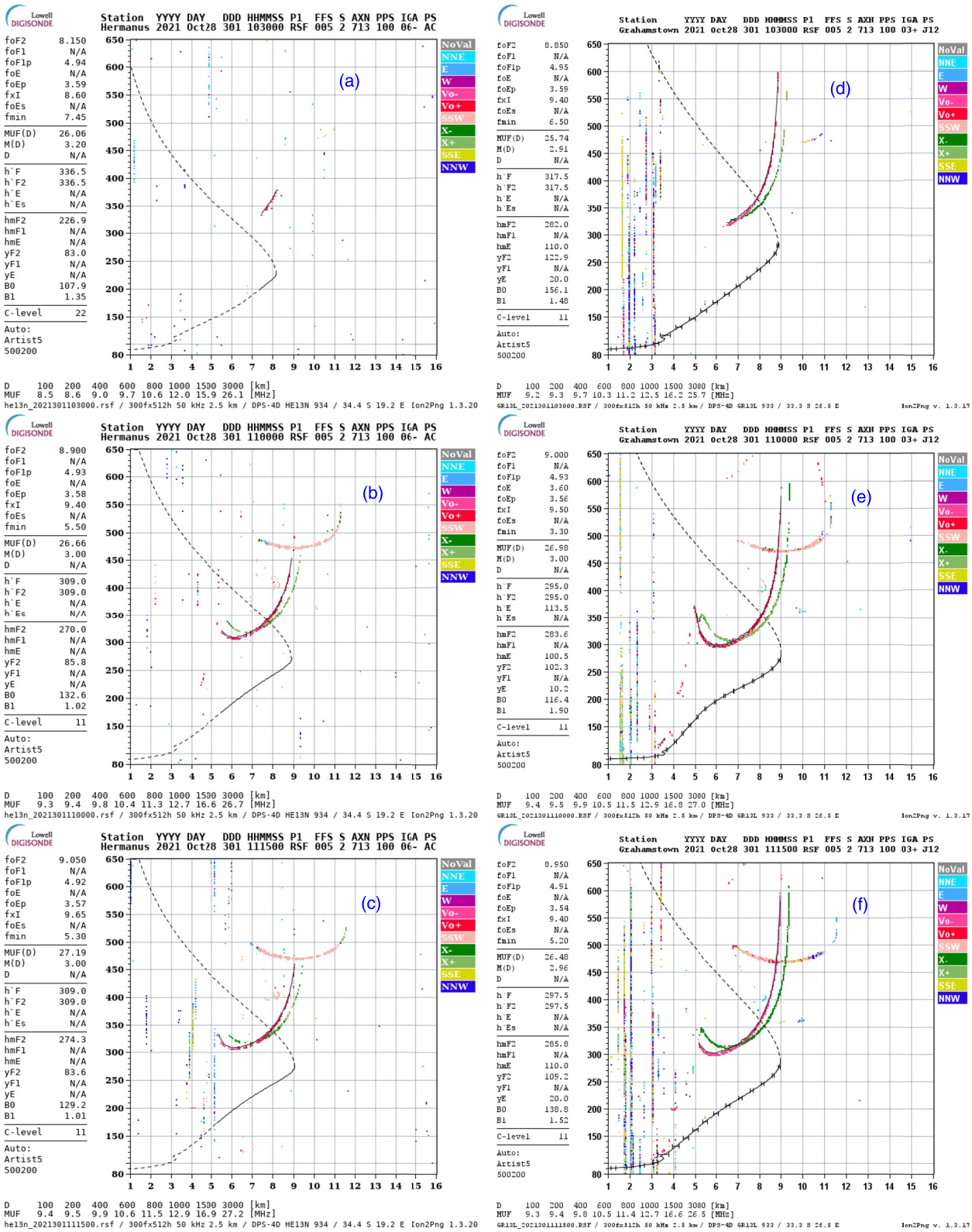

Figure 7. Examples of ionograms showing the effect of M2.2 solar flare on the E and F1 frequencies over HE13N (a–c) and GR13L (e–f) at 1030 UT 1100 UT and 1115 UT on 28 October 2021.

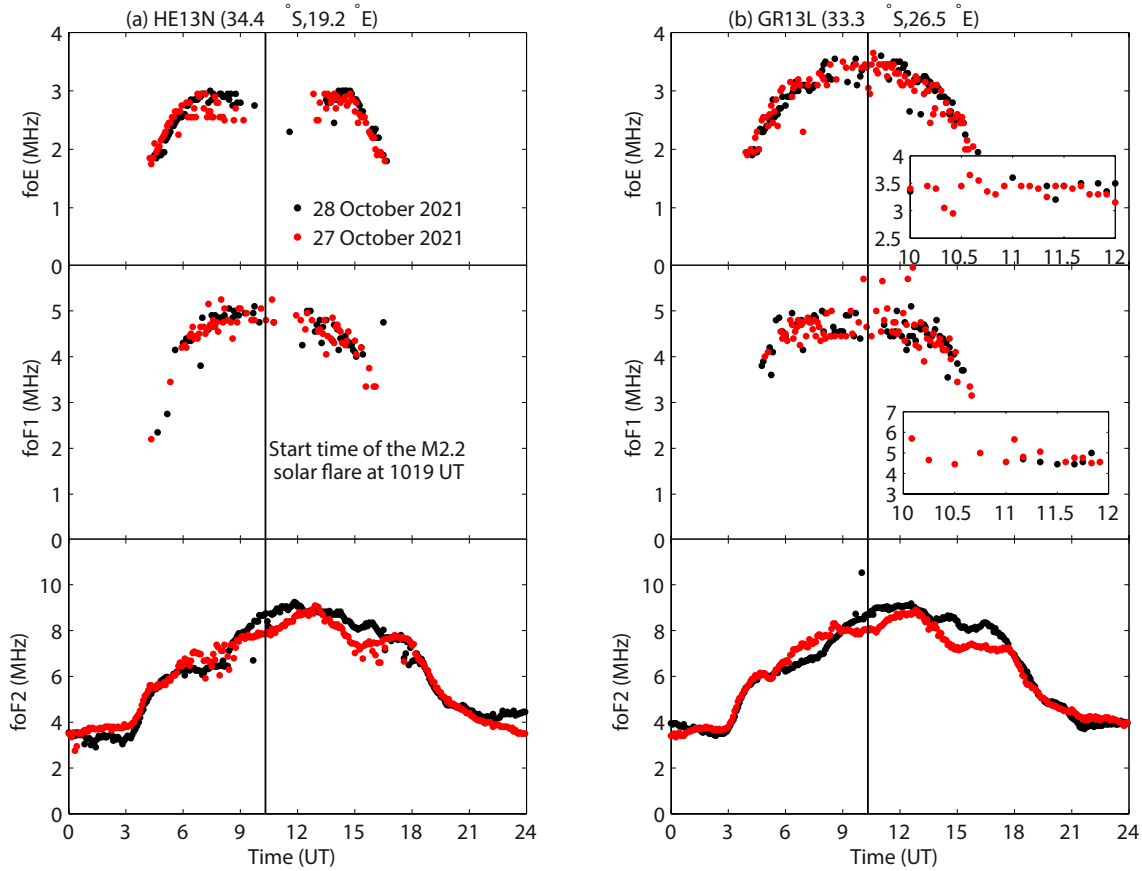

Figure 8. Diurnal variation of foE, foF1 and foF2 on 28 October 2021 (black dots) over (a) Hermanus (34.4°S, 19.2°E) and (b) Grahamstown (33.3°S, 26.5°E). The red dots show foE, foF1 and foF2 over both ionosonde locations on 27 October 2021. The vertical black line indicates the start time of the M2.2 solar flare at 1019 UT.

For the X1.0 solar flare which started at 1517 UT, we note that HF echoes from the F1 layer were present at 1520 UT over GR13L on 28 October 2021. After this time, no traces of F1 layer were observed again for the rest of the day. The situation over HE13N was slightly different in a sense that HF echoes from both F1 and E layers were clearly present until 1525 UT. Thereafter, echoes from both of these layers disappeared until 1555–1640 UT when O traces of the E layer are observed. Detailed ionograms can be found in the Supporting Information S1.

Figure 8 shows diurnal variations of foE, foF1 and foF2 over HE13N and GR13L on 28 October 2021. Plotted in red color are the respective parameters on the geomagnetically quiet day of 27 October 2021 for comparative purposes. The vertical black line shows the start of the M2.2 solar flare at 1019 UT. Analysis of foF2 over both HE13N and GR13L showed that not all the F2-layer frequencies were absorbed due to all the three solar flares including the X1.0 class which started at 1517 UT and ended at 1548 UT. Therefore the F2 layer was available at all times during the duration of the investigated solar flares. However, further investigations revealed that all the three solar flares had an impact on E and F1 frequencies. In fact, the M2.2 class solar flare which lasted for 18 min (1019–1037 UT) had a considerable influence on both E and F1 layer frequencies. Figure 8a shows that there was no foE data over HE13N for both 27 and 28 October 2021 during about 0900–1300 UT. While this was partly related to occurrence of solar flare on 28 October 2021, there was significant spreading in frequencies (in E and F1 layers) on 27 October 2021 during this time, making it difficult to accurately determine foE and foF1 parameters. It is clear that the F1 layer was unavailable immediately after the start of the M2.2 solar flare until 1200 UT over HE13N as shown in Figure 8a. For GR13L, the picture of the solar flare effects especially the M2.2 class is clearer as observed from foE and foF1 observations in Figure 8b during 1000–1115 UT. This is well demonstrated by the magnified insets for foE and foF1 plots in Figure 8b during 1000–1200 UT. During this time interval, the 27 October 2021 (red dots) shows almost all data, while the gaps evident in the 28 October 2021 data are due to the M2.2 solar flare.

While the two M and one X class solar flares of 28 October 2021 did not lead to total radio blackout and HF communication was still feasible over the African region, it was only restricted to the F2 region especially during the M2.2 solar flare. The design of sky wave propagation modes may involve single or multiple hops (Davies, 1990; McNamara, 1991) based on the users' needs. During the duration of the M2.2 solar flare which made radio wave propagation in the HF range using E and F1 layers unavailable for about 2 hr, complex propagation paths such as double hop through F and E (1F1E) regions were practically impossible. Establishing this is particularly important for space weather monitoring and forecasting in terms of knowing the flare magnitudes' influence on a range of frequencies as well as the duration, thus leading to accurate specification of HF communication.

4. Discussion

Experimental and theoretical studies of solar flares' effects on the ionosphere have been ongoing for decades (e.g., Hernández-Pajares et al., 2012; Liu et al., 2004; Mitra, 1974; Prölss, 2004; Tsugawa et al., 2007; Tsurutani et al., 2005, and references therein) and our detailed understanding continues to improve based on new datasets, instrumentation and methodologies. This study focused on establishing the ionospheric effects during the two M and one X class flares that peaked at 0740, 1028 and 1535 UT on 28 October 2021 for the M1.4, M2.2 and X1.0, respectively over the African region. While it has not been straight forward to observe the effects of the M1.4 solar flare which peaked at 0740 UT on TEC (see Figure 3c) perhaps due to low ionization levels associated with the respective local time (about 0940 LT), ionogram data revealed partial blackout (for E and F1 layers) lasting about 10 min over GR13L, while only the E layer was affected over HE13N. A clear effect on TEC and lower ionospheric layers manifested for the M2.2 solar flare. From ionosonde data, both E and F1 layers were affected during the M2.2 solar flare for a duration reaching atmost 2 hr especially over HE13N. Around the M2.2 flare peaktime, the subsolar point was over the African region (13.27°S, 18.95°E) and the corresponding local time of 1228 LT signify that the ionosphere was directly sunlit over our region of study. It is known that the ionospheric effects are more pronounced around noon-time when the solar zenith angle is close to zero (e.g., Barta et al., 2019; Le et al., 2013; Tsurutani et al., 2005, and references therein). It has been shown that the TEC response during solar flares on the dayside hemisphere is highly dependent on the solar zenith angle (e.g., Le et al., 2013; Liu et al., 2004; Hernández-Pajares et al., 2012; Tsugawa et al., 2007). For-example, high values of detrended vertical TEC rate were obtained for increasing values of the cosine of solar zenith angle (χ) for both X and M class flares (Hernández-Pajares et al., 2012). Additionally, Le et al. (2013) showed a statistical linear relationship between ΔTEC and cosine of χ for X class solar flares which occurred during 1999–2006, as well as ΔTEC increase with decreasing χ. Taking an example of TEC deviations from their respective monthly median values at the peak of the X1.0 solar flare (1535 UT), we observe percentage deviations of 20%, 9% and 2% over ZAMB ($\chi = 55.81°$), HNUS ($\chi = 56.04°$) and MAL2 ($\chi = 57.98°$), respectively. This agrees with existing studies which have reported high TEC response to solar flares with respect to decreasing χ values (with exception of GRMA ($\chi = 55.53$) where the deviation was 5% at 1028 UT in this study). At this time, there was practically no major deviations seen at RAMO and MERS where the χ values were 70.74° and 73.71°, respectively. A small χ value over a particular location implies more high radiation flux penetration into the ionosphere or upper atmosphere resulting into increased ionization levels and ultimately leading to higher TEC deviations from the reference background.

There has been an observed TEC depletion (Figure 3c) at ≈15–25°S and ≈15–30°N geomagnetic latitude around and after the peak time (about 1735 LT) of the X1.0 solar flare. Previous and recent progress in related studies associate this observation to equatorial latitude electrodynamics in response to solar flare induced processes. Observational and simulation studies have revealed decreased daytime vertical $\mathbf{E} \times \mathbf{B}$ drift during solar flares (e.g., Chen et al., 2021; Liu, Qian, et al., 2021; Liu, Wang, et al., 2021; Qian et al., 2012; Zhang et al., 2017, and references therein). Statistical results showed increased equatorial electrojet (EEJ) and reduced vertical $\mathbf{E} \times \mathbf{B}$ drift (equatorial electric field, EEF) over Jicamarca (Zhang et al., 2017). The increased EEJ and decreased EEF were interpreted in terms of greater increased Cowling conductivity as a result of the solar flare in a such way that current continuity is maintained according to Ohm's law (e.g., Liu, Qian, et al., 2021; Liu, Wang, et al., 2021; Zhang et al., 2017). The effect of decreased EEF (vertical $\mathbf{E} \times \mathbf{B}$ drift) would then be the weakened fountain effect resulting into decreased TEC at the anomaly crests. However, Chen et al. (2021) recently showed that the decreased daytime EEF during solar flares extends from equatorial to low as well as mid-latitudes (see

their Figure 6). According to Chen et al. (2021), during the solar flare which increases the E-region conductivity, the suppression of the F-region dynamo effect exceeds the strengthening of the E-region dynamo resulting in decreased daytime EEF and hence vertical $\mathbf{E} \times \mathbf{B}$ drift. Despite the unavailability of EEJ and EEF data over the 20–40°E longitude sector during the X1.0 solar flare of 28 October 2021, the observed TEC depletion at ≈15–25°S and ≈15–30°N geomagnetic latitude is potentially linked to flare induced ionospheric electrodynamics (for a detailed description of the mechanism, please consult Chen et al., 2021).

With reference to median values of the four most geomagnetically quiet days, the deviation of 7%–12% at peak time of 1028 UT translates into TEC increase of 1.6–3 TECU induced by the M2.2 solar flare. For contextual purposes, Yasyukevich et al. (2018) reported a TEC increase of 3–4 TECU and 8–10 TECU for the X2.2 and X9.3 solar flares at mid latitudes for the 6 September 2017. In their analyses, Yasyukevich et al. (2018) reference their TEC variations during the solar flare to average of vertical TEC for two days prior to the solar flare day. Earlier, it was reported that intense solar flares such as X28 of 4 November 2003 (which has been suggested to have been X45) led to TEC increase reaching 7 TECU (Tsurutani et al., 2005) when compared to TEC a day before the flare day. However, based on a similar procedure, a less intense solar flare X17 of 28 October 2003 caused TEC increase reaching 25 TECU leading to a conclusion that the responsible mechanism for the observed TEC increase in both E and F layers was the extreme ultra violet (EUV) radiation (Tsurutani et al., 2005, 2009). In agreement with EUV as the major contributor of the ionizing radiation, Kunitsyn et al. (2015) also showed that the ionospheric response as a result of the X28 flare of 4 November 2003 was less intense than the X10 and X17 solar flares of 29 and 28 October 2003, respectively. In terms of rate of change of TEC, the X10 and X17 flares led to TEC variation rates of 4 TEC/min and 11 TEC/min, respectively compared to 1.38 TECU/min for the X28 solar flare. Other sources have pointed out that during solar flares, the main and dominant source of atmospheric heating and ionization is the solar EUV and not X-ray flux (e.g., Le et al., 2013). In absolute terms, it is difficult to directly compare TEC increases in various studies based on solar flare classes as the methodology in determining TEC deviations as well as main source of ionospheric ionization may be different. There is however a broader scientific consensus and understanding that different solar flare intensities lead to different ionospheric effects in both magnitude and duration. Thus, the fact that the strength of the flare based on X-ray radiation may not necessarily be a direct measure in terms of intensity of the ionospheric F region response (e.g., Kunitsyn et al., 2015; Le et al., 2013; Tsurutani et al., 2005, 2009), makes the investigation of each solar flare effects on the ionosphere a worthwhile effort for both fundamental and practical applications.

We have found a statistical agreement in the TEC enhancement as observed from bottomside ionosphere and GNSS observations. For-example, at the peaktime of the M2.2 solar flare, TEC increases as quantified from GNSS data over Grahamstown and Hermanus reached 12% and 7% respectively. Comparatively, BTEC increases just after the solar flare peak time (during the period of E and F1 layers' absence) were on average 13% and 8% over GR13L and HE13N, respectively. This may highlight the dominant role played by the EUV radiation at F2 layer heights during the M2.2 solar flare duration as opposed to the X-ray flux which was only effective in the lower ionospheric layers. The EUV radiation's role in causing more photoionization over GR13L than HE13N during this time interval is consistent with the expected ionosphere's diurnal variability with respect to local time. At longitudes of 26.5°E (GR13L) and 19.2°E (HE13N), these locations have a local time difference of about 30 min.

Observations of ΔTEC at peak times of the solar flares on 28 October 2021 reveal different TEC behavior in southern and northern hemispheres. At about 1030 UT (see Figure 3c), there is for-example a simultaneous TEC increase in the latitude range 20°−40°S in the southern hemisphere which is not necessarily reflected in the northern hemisphere (see e.g., at 30°−45°N). A similar observation is clearer for the X1.0 solar flare where there is no corresponding TEC increase in northern hemisphere compared to the observations in the southern hemisphere. Previously, Tsugawa et al. (2007) showed a clear summer-winter hemispheric asymmetry in TEC increase due solar flares of M5 class and above during 2000–2006. These authors further showed that their observations correlated well with changes in the ratio of atomic oxygen to molecular nitrogen (O/N_2). While analyzing TEC response due to X class solar flares during 1999–2006, Le et al. (2013) attributed large TEC increases in equinoxes compared to solstices to seasonal differences in O/N_2 values. Thus, while the summer-winter hemisphere asymmetry of TEC increase due to solar flares has been reported for solar flares higher than M5 in 2000–2006 (Tsugawa et al., 2007) and X-class flares in 1999–2006 (Le et al., 2013), it is interesting that this observation remains valid for “weak” flares of even M2 category as demonstrated in this study for the 28 October 2021. We

think that an appropriate TEC detrending methodology may be necessary to identify such effect in details for "weak" solar flares. For this case, we have fitted TEC for each visible satellite to a fourth order polynomial and binned ΔTEC into 3° latitude by 6 min within a 20° longitude sector. For each bin, we then select the median ΔTEC as opposed to other methods as it eliminates extreme ΔTEC values. Therefore the TEC enhancements that are more pronounced in the summer southern hemisphere than winter northern hemisphere during solar flares of 28 October 2021 may be attributed to seasonal differences in background neutral density (e.g., Tsugawa et al., 2007; Le et al., 2013).

5. Conclusions

Analysis of ionospheric response during the occurrence of M and X class solar flares on 28 October 2021 has shown that the F2 layer was still available for HF communication. However, HF propagation using the E and F1 layers was significantly affected and in some instances completely unavailable for over 2 hr as was the case during the M2.2 solar flare which peaked at 1028 UT (about 1228 local time over the longitude sector used in analysis). Due to the absorption in the *D* region which impacted the HF propagation in the F1 and E layers during the duration (and immediately after, lasting 2 hr) of the M2.2 solar flare, HF communication modes involving usage of two ionospheric layers such as 1F1E were not possible. At the peak of the M2.2 solar flare which occurred during 1019–1037 UT (1219–1237 local time), TEC increased in the range of 7%–12% over the background quiet time TEC in the southern hemispheric part of the African sector. The solar flare effects on ionospheric parameters are more pronounced in the summer southern hemisphere compared to winter northern hemisphere due to the background neutral density (e.g., Le et al., 2013; Tsugawa et al., 2007).

Data Availability Statement

Ionosonde data can be obtained from www.sansa.org.za and https://giro.uml.edu/. The GNSS observations are provided by the University Navstar Consortium, UNAVCO (https://www.unavco.org/data/gps-gnss/gps-gnss.html and ftp://data-out.unavco.org) and South African National Geospatial Information (www.trignet.co.za and ftp://ftp.trignet.co.za). GOES X-ray data can be found on http://www.ngdc.noaa.gov/stp/satellite/goes/index.html. Solar wind parameters were obtained from https://spdf.gsfc.nasa.gov/pub/data/omni/high-res-omni/. Kp and Dst indices were downloaded from https://omniweb.gsfc.nasa.gov/form/dx1.html. The Kp index is derived and distributed by GFZ Potsdam (Matzka et al., 2021), while the Dst index is provided by World Data Center, Kyoto, Japan (https://wdc.kugi.kyoto-u.ac.jp/dstae/index.html).

Acknowledgments
This work is based on the research supported in part by the National Research Foundation of South Africa (Grant Nos. 116005 and 129285) and opinions, findings and conclusions or recommendations expressed in this paper are of the author(s), and the NRF accepts no liability whatsoever in this regard.

References

Barta, V., Sátori, G., Berényi, K. A., Williams Kis, Á. E., & Williams, E. (2019). Effects of solar flares on the ionosphere as shown by the dynamics of ionograms recorded in Europe and South Africa. *Annales Geophysicae*, *37*(4), 747–761. https://doi.org/10.5194/angeo-37-747-2019

Blagoveshchensky, D. V., & Sergeeva, M. A. (2019). Impact of geomagnetic storm of September 7-8, 2017 on ionosphere and HF propagation: A multi-instrument study. *Advances in Space Research*, *63*(1), 239–256. https://doi.org/10.1016/j.asr.2018.07.016

Chen, J., Lei, J., Wang, W., Liu, L., Maute, A., Qian, L., et al. (2021). Ionospheric electrodynamic response to solar flares in September 2017. *Journal of Geophysical Research: Space Physics*, *126*(11), e2021JA029745. https://doi.org/10.1029/2021JA029745

Curto, J. J., Marsal, S., Blanch, E., & Altadill, D. (2018). Analysis of the solar flare effects of 6 September 2017 in the ionosphere and in the Earth's magnetic field using spherical elementary current systems. *Space Weather*, *16*(11), 1709–1720. https://doi.org/10.1029/2018SW001927

Davies, K. (1990). *Ionospheric radio*. Peter Peregrinus.

Fagundes, P. R., Pezzopane, M., Habarulema, J. B., Venkatesh, K., Dias, M. A. L., Tardelli, A., et al. (2020). Ionospheric disturbances in a large area of the terrestrial globe by two strong solar flares of September 6, 2017, the strongest space weather events in the last decade. *Advances in Space Research*, *66*(7), 1775–1791. https://doi.org/10.1016/j.asr.2020.06.032

García-Rigo, A., Hernández-Pajares, M., Juan, J. M., & Sanz, J. (2007). Solar flare detection system based on global positioning system data: First results. *Advances in Space Research*, *39*(5), 889–895. https://doi.org/10.1016/j.asr.2006.09.031

Habarulema, J. B., Katamzi-Joseph, Z. T., Buresova, D., Nndanganeni, R., Matamba, T., Tshisaphungo, M., et al. (2020). Ionospheric response at conjugate locations during the 7–8 September 2017 geomagnetic storm over the Europe-African longitude sector. *Journal of Geophysical Research: Space Physics*, *125*(10), e2020JA028307. https://doi.org/10.1029/2020JA028307

Hernández-Pajares, M., García-Rigo, A., Juan, J. M., Sanz, J., Monte, E., & Aragón-Àngel, A. (2012). GNSS measurement of EUV photons flux rate during strong and mid solar flares. *Space Weather*, *10*(12), S12001. https://doi.org/10.1029/2012SW000826

Huang, X., & Reinisch, B. W. (2001). Vertical electron content from ionograms in real time. *Radio Science*, *36*(2), 335–342. https://doi.org/10.1029/1999rs002409

Kelley, M. C., Fejer, B. G., & Gonzales, C. A. (1979). An explanation for anomalous equatorial ionospheric electric fields associated with a northward turning of the interplanetary magnetic field. *Geophysical Research Letters*, *6*(4), 301–304. https://doi.org/10.1029/GL006i004p00301

Kunitsyn, V. E., Nazarenko, M. O., Nesterova, I. A., & Padokhin, A. M. (2015). Solar flare forcing on ionization of the upper atmosphere. Comparative study of several major X-class events of 23rd and 24th solar cycles. *Moscow University Physics Bulletin*, *70*(4), 312–318. https://doi.org/10.3103/S0027134915040128

Le, H., Liu, L., Chen, Y., & Wan, W. (2013). Statistical analysis of ionospheric responses to solar flares in the solar cycle 23. *Journal of Geophysical Research: Space Physics*, *118*(1), 576–582. https://doi.org/10.1029/2012ja017934

Liu, J., Qian, L., Maute, A., Wang, W., Richmond, A. D., Chen, J., et al. (2021). Electrodynamical coupling of the geospace system during solar flares. *Journal of Geophysical Research: Space Physics*, *125*(1), e2020JA028569. https://doi.org/10.1029/2020JA028569

Liu, J., Wang, W., Qian, L., Lotko, W., Burns, A. G., Pham, K., et al. (2021). Solar flare effects in the Earth's magnetosphere. *Nature Physics*, *17*(7), 807–812. https://doi.org/10.1038/s41567-021-01203-5

Liu, J. Y., Lin, C. H., Tsai, H. F., & Liou, Y. A. (2004). Ionospheric solar flare effects monitored by the ground-based GPS receivers: Theory and observation. *Journal of Geophysical Research*, *109*(A1), A01307. https://doi.org/10.1029/2003JA009931

Matzka, J., Bronkalla, O., Tornow, K., Elger, K., & Stolle, C. (2021). Geomagnetic Kp index. V. 1.0. *GFZ Data Services*. https://doi.org/10.5880/Kp.0001

McNamara, L. F. (1991). *The ionosphere: Communications, surveillance and direction finding*. Krieger Publishing Company.

Mitra, A. P. (1974). *Ionospheric effects of solar flares*. D. Reidel Publishing Company.

Mosna, Z., Kouba, D., Knizova, P. K., Buresova, D., Chum, J., Sindelarova, T., et al. (2020). Ionospheric storm of September 2017 observed at ionospheric station Pruhonice, the Czech Republic. *Advances in Space Research*, *65*(1), 115–128. https://doi.org/10.1016/j.asr.2019.09.024

Prölss, G. W. (2004). *Physics of the Earth's space environment*. Springler-Verlag.

Qian, L., Burns, A. G., Solomon, S. C., & Chamberlin, P. C. (2012). Solar flare impacts on ionospheric electrodynamics. *Geophysical Research Letters*, *39*(6), L06101. https://doi.org/10.1029/2012GL051102

Seemala, G. K., & Valladares, C. E. (2011). Statistics of total electron content depletions observed over the South American continent for the year 2008. *Radio Science*, *46*(5), RS5019. https://doi.org/10.1029/2011RS004722

Thomson, N. R., Rodger, C. J., & Dowden, R. L. (2004). Ionosphere gives size of the greatest solar flare. *Geophysical Research Letters*, *31*(6). https://doi.org/10.1029/2003GL019345

Tsugawa, T., Zhang, S.-R., Coster, A. J., Otsuka, Y., Sato, J., Saito, A., et al. (2007). Summer-Winter hemispheric asymmetry of the sudden increase in ionospheric total electron content and of the O/N_2 ratio: Solar activity dependence. *Journal of Geophysical Research*, *112*(A8), A08301. https://doi.org/10.1029/2007JA012415

Tsurutani, B. T., Judge, D. L., Guarnieri, F. L., Gangopadhyay, P., Jones, A. R., Nuttall, J., et al. (2005). The October 28, 2003 extreme EUV solar flare and resultant extreme ionospheric effects: Comparison to other Halloween events and the Bastille Day event. *Geophysical Research Letters*, *32*(3), L03S09. https://doi.org/10.1029/2004GL021475

Tsurutani, B. T., Verkhoglyadova, O. P., Mannucci, A. J., Lakhina, G. S., Li, G., & Zank, G. P. (2009). A brief review of "solar flare effects" on the ionosphere. *Radio Science*, *44*(1), 1–14. https://doi.org/10.1029/2008RS004029

Valladares, C. E., Villalobos, J., Hei, M. A., Sheehan, R., Basu, S., MacKenzie, E., et al. (2009). Simultaneous observation of traveling ionospheric disturbances in the Northern and Southern Hemispheres. *Annales Geophysicae*, *27*(4), 1501–1508. https://doi.org/10.5194/angeo-27-1501-2009

Yasyukevich, Y., Astafyeva, E., Padokhin, A., Ivanova, V., Syrovatskii, S., & Podlesnyi Liu, A. (2018). The 6 September 2017 X-class solar flares and their impacts on the ionosphere, GNSS, and HF radio wave propagation. *Space Weather*, *16*(8), 1013–1027. https://doi.org/10.1029/2018SW001932

Zhang, R., Liu, L., Le, H., & Chen, Y. (2017). Equatorial ionospheric electrodynamics during solar flares. *Geophysical Research Letters*, *44*(10), 4558–4565. https://doi.org/10.1002/2017GL073238